JOURNAL OF SYNCHROTRON RADIATION
ISSN 1600-5775

Refraction and ultra-small-angle scattering of X-rays in a single-crystal diamond compound refractive lens

S. Gasilov,[a]* A. Mittone,[b] T. dos Santos Rolo,[a] S. Polyakov,[c] S. Zholudev,[c] S. Terentyev,[c] V. Blank,[c] A. Bravin[b] and T. Baumbach[a,d]

[a]Institute for Photon Science and Synchrotron Radiation, Karlsruhe Institute of Technology (KIT), Eggenstein, Germany, [b]European Synchrotron Radiation Facility, Grenoble, France, [c]Technological Institute for Superhard and Novel Carbon Materials, Troitsk, Russian Federation, and [d]Laboratory for Applications of Synchrotron Radiation, Faculty of Physics, Karlsruhe Institute of Technology (KIT), Karlsruhe, Germany. *Correspondence e-mail: sergey.gasilov@lightsource.ca

Received 23 May 2017
Accepted 6 September 2017

Edited by A. Momose, Tohoku University, Japan

Keywords: compound refractive lens; single-crystal diamond; aberrations; ultra-small angle X-ray scattering; rocking-curve imaging.

In this work a double-crystal setup is employed to study compound refractive lenses made of single-crystal diamond. The point spread function of the lens is calculated taking into account the lens transmission, the wavefront aberrations, and the ultra-small-angle broadening of the X-ray beam. It is shown that, similarly to the wavefront aberrations, the ultra-small-angle scattering effects can significantly reduce the intensity gain and increase the focal spot size. The suggested approach can be particularly useful for the characterization of refractive X-ray lenses composed of many tens of unit lenses.

1. Introduction

The outstanding thermal conductivity of single-crystal diamond makes this material particularly attractive for the realisation of compound refractive X-ray lenses (CRLs) for collimation and focusing of high-power X-ray beams (Snigirev *et al.*, 2002). In addition, unlike polycrystalline materials, single-crystal diamond should not produce a noticeable scattering pattern that can interfere, for instance, with small-angle-scattering experiments. However, diamond is very difficult to process because of its hardness. Only recently refractive X-ray lenses with rotational parabolic surfaces have been manufactured out of diamond single-crystals; milling by means of material ablation with ultrafast laser pulses was used to process the diamond (Terentyev *et al.*, 2015). Since then, results of several more trials have been reported, where diamond single-crystal CRLs were used to focus an X-ray beam produced by an undulator source (see also Antipov *et al.*, 2016; Terentyev *et al.*, 2017). In all experiments it was found that in the supposed image plane the intensity profile of the beam deviated from the expected figure. However, only general conclusions on the origin of this effect have been reported, such as that aggregate errors in the unit lenses' surface shape, a limited stacking precision, and surface roughness were the sources of imperfections (Terentyev *et al.*, 2015; Antipov *et al.*, 2016). In this work we undertake a detailed study of single-crystal diamond X-ray lenses manufactured by the Technological Institute for Superhard and Novel Carbon Materials (TISNCM) in Troitsk, Russia (Terentyev *et al.*, 2015).

CRLs are often used to increase the photon flux density on a sample, and, in that case, the intensity gain is an important measure of the CRL quality. It is normally expressed in terms of the CRL transmission and its effective aperture, which are

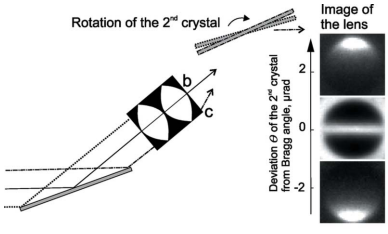

related to the attenuation of X-rays in the lens. In this work we follow definitions introduced by Snigirev *et al.* (1998) and Lengeler *et al.* (1998): the gain is a dimensionless parameter equal to the ratio of the intensity in the focal spot of the lens and the intensity in an equal area without the lens; in the established model, the gain is proportional to the CRL transmission. The effective aperture is the diameter of the effectively transmitting surface of the CRL, and it is always smaller than the geometrical aperture due to the absorption and scattering of X-rays. Frequently, the testing of a CRL consists of a series of X-ray beam intensity measurements performed by means of a high-spatial-resolution X-ray detector and slits placed at single or multiple positions after the CRL (see Piestrup *et al.*, 2000; Stöhr *et al.*, 2015; Antipov *et al.*, 2016; *etc.*, and references therein). Besides, some studies include measurements of the small-angle-scattering profiles produced by the lens material (Lengeler *et al.*, 1998; Semenov *et al.*, 2017). Small-angle scattering can increase the apparent attenuation coefficient, which subsequently reduces the achievable gain; also, as noted before, the scattering pattern produced by the CRL can interfere with genuine experimental data. In addition to the mentioned experiments, several studies have addressed the problem of the wavefront aberrations in the exit pupil of a refractive X-ray lens. Such information can be very important in microscopy experiments when CRLs are used to create a magnified image of an object; furthermore, severe aberrations can significantly blur the focal spot and decrease the intensity gain. However, so far aberrations produced by a single unit lens have been studied (Weitkamp *et al.*, 2005; Rutishauser *et al.*, 2011; Koch *et al.*, 2016). While such data provide a useful insight into geometrical errors in the shape of a unit lens, aggregate effects produced by stacking of many unit lenses can be different. Recently, ptychography (Seiboth *et al.*, 2016, 2017) has been successfully applied to characterize aberrations in a CRL.

In order to study simultaneously the attenuation, refraction and scattering of X-rays in a CRL, we employed a double-crystal setup (DCS) method. The DCS method consists of measuring the double-crystal rocking curve with and without an object placed between two crystals (Wernick *et al.*, 2003). Changes in the rocking curve are related to absorption and angular deflection of X-rays in the examined object. The DCS technique can also cope with the large wavefront curvatures induced by a stack of unit X-ray lenses. We have carried out measurements using 51 keV X-rays, because at this energy the wavefront curvatures become suitably small. The wavefront at the target energy can be obtained then by a simple scaling with the Lorentz dispersion formula (Slack, 1926). This approach is validated by comparison with the results derived from the tomographic imaging of the CRL assembly. Results of tomography examination are given in §2, while a detailed description of the DCS technique is provided in §3.

§4 is devoted to a discussion on directly resolved surface imperfections and associated wavefront aberrations. These wavefront aberrations stem from systematic surface errors, which can be removed by making appropriate adjustments in the manufacturing process. In addition, these results can be used to simulate propagation of an X-ray beam after the CRL. In this way, the angular width of the focal spot as it is seen from the lens exit pupil was estimated.

DCS measurements also yield information about the distribution of the transmitted beam intensity in the angular interval comparable with angular dimensions of the focal spot. This is discussed in §5. First, it is possible to find the fraction of photons that is lost due to the small-angle scattering on inhomogeneities inside the CRL (Parratt *et al.*, 1959). These photons do not contribute to the image formation, which can be considered as the increase of the apparent attenuation coefficient of the CRL or, likewise, the decrease of the CRL transmissivity. Secondly, changes in the angular distribution of the beam intensity comparable with the angular width of the focal spot must affect the spatial profile of the beam intensity at the focal spot. We have observed a steady angular broadening of the transmitted beam as the number of unit lenses in the stack increases. This effect can be explained by the multiple refraction of X-rays on the imperfect surfaces of unit lenses (von Nardroff, 1926; Faris & Byer, 1988).

The scaling of the X-ray scattering angle and of the broadening due to multiple refraction with the photon energy is a known phenomenon (Beeman & Kaesberg, 1947). Therefore, obtained refraction and scattering data for 51 keV X-rays can be used to assess the performance of the CRL at a different photon energy. In §6 we have evaluated the response of a nine-lens CRL to a 15 keV beam; this energy was selected because it is close to the typical operation conditions of the CRL. The influence of aberrations and ultra-small-angle scattering on the optical properties of the CRL were compared by calculating the point spread function (PSF) of the CRL taking each effect subsequently into account. Predictably, detected geometrical errors in the unit lens shape, whose spatial scales exceed the detector resolution, worsen the optical quality of the CRL; namely, the width of the PSF increases by a factor of two if wavefront aberrations are taken into account in addition to the CRL transmission. The CRL transmission is not substantially affected by the small-angle scattering, as it was expected from the homogeneity of the single-crystal diamond. However, the multiple refraction and ultra-small-angle scattering on imperfections, whose spatial scale is below the detector resolution, produce an effect comparable with the large-scale geometrical errors. This fact could severely impair the performance of CRLs composed of many tens of diamond lenses manufactured by laser milling.

2. Structure of the CRL

In this section we describe the unit lens and the structural properties of lens stacks that have been deduced from an X-ray microtomography (μCT) examination. Each unit lens is made out of diamond single-crystal shaped as a cylinder with diameter 1.5 mm and height 0.5 mm [see Terentyev *et al.* (2015) and Kolodziej *et al.* (2016) for details on the growing process and laser micromachining]. Concave lens surfaces are defined by a paraboloid of revolution with the radius of curvature R_t = 200 μm at its vertex. The diameter of the

geometric lens aperture is equal to 0.9 mm; its center coincides with the crystal central axis. To stack the unit lenses together, a guiding duct was drilled into an acrylic puck which served as the CRL casing. The diameter of this duct closely matches the outer diameter of diamond crystals. CRLs were then assembled by pressing lenses one after another into this duct. The absence of plastic curls or other debris in the lens aperture was controlled using an optical microscope.

Properties of the CRL were studied repeatedly using the DCS setup when the number of lenses in the CRL stack was equal to 1, 2, 5 and 9. In addition, the μCT imaging of the resulting nine-lens stack was carried out using a polychromatic X-ray beam produced by a bending-magnet source at the Topo-Tomo beamline of the ANKA synchrotron (KIT, Germany). The mean photon energy E of the beam is about 15 keV after filtering with an Al plate. That Al filter and a beryllium window are the two sole elements between the source and the sample, which assures homogeneous illumination of the sample. The X-ray imaging detector was composed of a PCO.dimax camera mounted on a lens system connected to a LSO:Tb scintillator. The effective pixel size was 1.2 μm × 1.2 μm. The computed tomography (CT) axis coincided with the main optical axis of the CRL.

The analysis of the μCT images allows the conclusion that the lens material is homogeneous: neither cracks nor voids were detected inside the processed diamond crystals. An X-ray projection image is shown in Fig. 1(*a*). It can be seen that contours of parabolic surfaces are emphasized by a black fringe owing to Fresnel diffraction. A segmentation procedure was performed with the aid of these fringes. The resulting distribution of voids in a plane containing the CRL central axis is shown in Fig. 1(*b*) for a fragment consisting of five

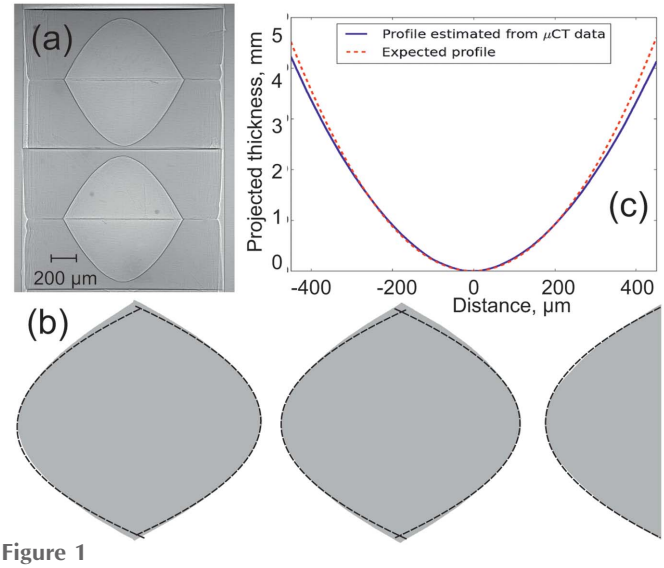

Figure 1
X-ray image of four plano-concave lenses in the holder (*a*); edges of the parabolic surface are highlighted due to Fresnel diffraction. Distribution of hollows in the symmetry plane (*b*); ideal parabolic curves, shown with dotted lines, are superimposed on image (*b*) to illustrate systematic deviation from the expected profile. Projected thickness of diamond in the lens exit plane (*c*). The discrepancy between expected and calculated profile is very pronounced at the peripheral part of the lens.

plano-concave lenses. Contours of the segmented surfaces are compared against the profile of an ideal parabola with the radius of curvature $R = R_t$. A systematic error in the lens shape is clearly visible: the slope of the parabolic surface increases more slowly than it should; this discrepancy becomes very large at the peripheral part of the lens. The fitting of the segmented surfaces with a parabola was also used to assess the alignment errors of unit lenses with respect to the main CRL axis. It was found that the displacement of the parabolas' vertices in the plane perpendicular to the optical axis does not exceed $d < 20$ μm. The mean value of the displacement satisfies a tolerance relation for unit lens alignment in a CRL assembly (Pantell *et al.*, 2001). The angular misalignment ϑ, *i.e.* the tilt between the axis of a unit lens and the CRL axis, is smaller than 0.01 rad. It can be shown that in the first-order approximation this angular error is equivalent to the variation of the lateral position of the parabolas' vertices. In our case the residual tilt of unit lenses introduces an error smaller than the lateral displacement error since $\vartheta < d/R_t \simeq 0.1$. We can thus conclude that the stacking precision is acceptable. The average thickness of the base of each lens (the distance from lens apex to the flat surface of the crystal) is found to be around 30 μm. That is in very good agreement with the design value.

The calculated projected thickness is show in Fig. 1(*c*). It is seen that the aggregate path-length error becomes quite large at peripheral points of the CRL pupil (see §4 for discussion). To estimate the angular deflection of X-rays in the lens exit plane, the extracted thickness of diamond T can be converted into the phase advance profile φ using the relation $\varphi = T\delta k$, where $\delta \simeq E^{-2}$ is the refractive index decrement and $k \simeq E$ is the wavenumber. Consequently, local deflection angles α are estimated using the central finite difference approximation to the first derivative of the phase. In terms of projected thickness it can be expressed as: $\alpha_i = (T_{i+1} - T_{i-1})\,\delta/2\Delta$, where i is the pixel index. The absolute error of such an estimation is ∼0.14 μrad. This depends on the detector pixel size Δ, which determines the minimum increment of the thickness. The relations $\alpha \simeq E^{-2}$ and $\varphi \simeq E^{-1}$ can be used to scale the phase delays and to compare magnitudes of deflection angles measured at different photon energy.

3. The double-crystal setup

Direct measurements of the X-ray deflection in the lens exit plane were carried out at biomedical beamline ID17 of the European Synchrotron Radiation Facility (ESRF, France). The basic principle of measurements made using the DCS is illustrated in Fig. 2(*a*). A collimated monochromatic beam illuminates a CRL placed between two plane, perfect crystals. The intensity I_{RC} of the beam transmitted through the CRL is measured after reflection of the beam from the second crystal as a function of the crystal angle θ and of the spatial coordinates: $I_{RC} = f(\theta, x, y)$. The detuning angle θ is defined as the deviation of the second (analyzer) crystal from the exact Bragg angle for the given beam energy; the (x, y) coordinates describe both a point in the CRL exit plane and the corre-

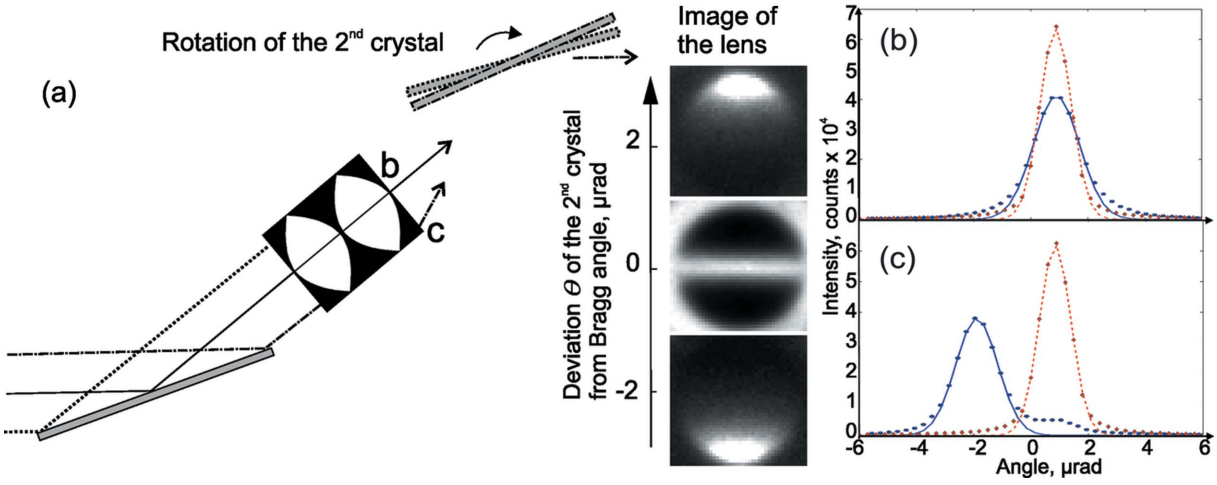

Figure 2
Sketch of the measurement procedure. Raw images of a nine-lens stack are shown at different analyzer crystal angles θ (*a*). The intensity *versus* angle distribution is obtained then for each pixel. Panels (*b*) and (*c*) show the function $I_{RC}(\theta)$ for 20 μm × 20 μm wavefront samples near the CRL optical axis and at the distance 260 μm far from it. In the former case the transmitted beam is not deflected from the initial propagation direction, while in the latter it does. Circle markers show the measured intensity, dashed lines depict the Gaussian fit of the reference RC and the solid line shows the fit with the CRL in place. The RC profile asymmetry that is seen in Fig. 2(*c*) is discussed in §5.

sponding detector pixel. If $\theta = 0$, only those rays which propagate in directions almost parallel to the lens optical axis contribute to the image. An example is shown in Fig. 2(*a*), where the ray 'b' remains undeflected because it entered the CRL on its optical axis. Peripheral rays, such as ray 'c' in Fig. 2(*a*), experience largest deflection and are not reflected by the second crystal. One needs to detune the analyzer crystal from the initial position $\theta = 0$ in order to meet the Bragg condition for these rays. The amount of rotation $d\theta$ at which the intensity in a pixel is maximized is equal to the mean angular deflection α of X-rays in a wavefront sample corresponding to that pixel. Rotation $d\theta$ is proportional to the deflection in the meridional plane of the CRL. In order to measure the amount of X-ray deflection in the sagittal plane it is necessary to repeat the measurements after the CRL is rotated by 90° around its optical axis. In this way the refractive properties of a sample placed between two crystals can be assessed. In practice, we record the whole series of X-ray images at different θ and then the function I_{RC} is analyzed pixel by pixel as function of θ. We will refer to the local intensity *versus* angle distribution $I_{RC} = f(\theta)$ measured at a point (x_i, y_j) as the rocking curve (RC). A reference RC is recorded without the lens placed between crystals in order to account for the global beam divergence and for the spatial variations of the beam intensity in the lens entrance plane. Pairs of I_{RC} measured near the lens optical axis and close to its circumference are shown by circle markers in Figs. 2(*b*) and 2(*c*).

It is seen in Fig. 2(*c*) that, besides a shift due to the transmitted beam deflection, the RC experiences other transformations when the X-ray lens is placed in between the crystals. In order to compare the reference and the object RC, we approximate them by a Gaussian function. Two RCs typical for central and peripheral points of the CRL pupil are shown in Figs. 2(*b*) and 2(*c*), respectively. Although the Gaussian fit does not allow the RC tails to be quantified, it gives a very good estimate of the intensity and position of the RC peak, and of the curve width; these parameters are related to the attenuation and scattering of X-rays in the sample. We extracted in total four quantities and considered their spatial distributions in the lens exit plane (Fig. 3).

Several conditions must be satisfied to perform the described experiment: (i) the spread of the incidence angles of X-rays on the detector pixel (the local beam divergence) has to be much smaller than the rocking curve width; (ii) the beam must be monochromatic and the energy dispersion along the crystal surface should be small; (iii) the intensity of lower (111) and higher-order reflections from the DCS crystals must be negligible. The configuration of the ID17 beamline fulfills these requirements. The DCS is located ∼150 m from the wiggler source. Silicon (333) reflections are used at 51 keV photon energy. Thus, first, the divergence of the X-ray beam

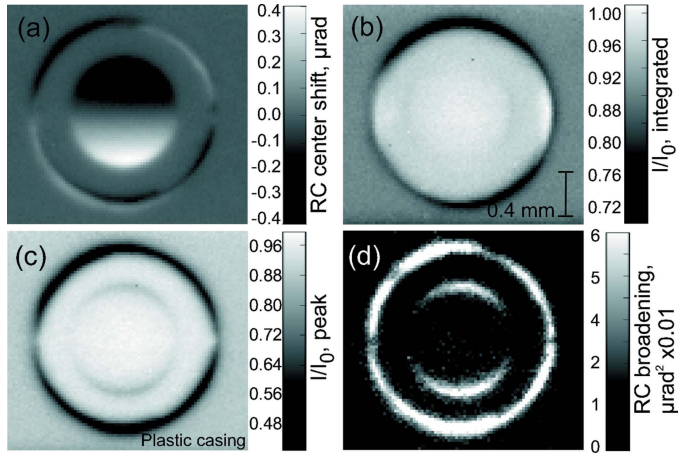

Figure 3
Two-dimensional distribution of $I_{RC}(\theta)$ parameters obtained for a unit lens: shift of the RC peak position (*a*), ratios of integrated (*b*) and peak (*c*) intensities of RCs taken with and without the CRL, respectively; and the increment of the RC variance (*d*).

within the wavefront sample with dimensions up to 100 μm × 100 μm is much smaller than the Darwin width of the Si (333) reflection. Second, after reflection from the first crystal the relative energy bandwidth of the beam is reduced to $\Delta E/E \simeq 10^{-5}$ with a negligible spatial dispersion of energy across the lens entrance pupil. Owing to this high degree of monochromaticity and an almost perfect collimation, the average half-width of the measured reference RC is 1.40 ± 0.05 μrad, which is very close to the minimum value of 1.33 μrad predicted by theory for the Si (333) double-crystal RC width (Stepanov, 2004). Finally, higher- and lower-order reflections do not interfere with measurements. The Si (111) reflection for 17 keV X-rays is eliminated by the primary beamline monochromator, which operates with (111) reflections in Laue geometry. The relative intensity of the 153 keV X-rays, which contribute to the next, most intense, higher-order reflection, is $<10^{-3}$ compared with the 51 keV X-rays and thus can be neglected.

With the given source divergence, the beam size at the sample position exceeds the entrance pupil of the lens, which is slightly less than 1 mm × 1 mm. The spread of the incidence angles over the entire lens entrance pupil is about 6 μrad. At E = 51 keV, the maximum expected value of the refraction angles is about 3 μrad. Furthermore, the CRL bends the X-ray trajectories in such a way that the global beam divergence decreases. Therefore, the scan range of the analyzer crystal was set to $\theta_{max} = \pm 6$ μrad from the Bragg angle. Within this interval, images of the lens were typically taken at 40 equidistant θ points.

The X-ray detector provides an effective pixel size of 20 μm × 20 μm. This resolution was chosen so that dimensions of the analyzed wavefront samples significantly exceed both the first Fresnel zone size and the transversal displacement of X-rays in the propagation from the CRL to the detector. The distance between the sample and detector was around 1 m, which determines the value of about 5 μm for the first Fresnel zone at 51 keV, so that the diffraction effects can be neglected for the selected pixel size. Next, taking typical deflection angles, one finds that the transversal displacement of the rays was around 3 μm. Therefore, to a very good approximation the wavefront fragments associated with each pixel can be analyzed independently of each other. It is worth noting that the spatial resolution of the setup could be improved by making the whole system more compact.

4. Refraction of the beam transmitted through the CRL

Fig. 4(*a*) presents, by means of a vector field, the 2D map of deflection angles in the exit plane of the nine-lens CRL. It was reconstructed from two components of the deflection measured in orthogonal directions as described in the previous section. Figs. 4(*b*) and 4(*c*) show the deflection angle error for points lying in the meridional and sagittal planes. The error is computed as the difference between measured values and the deflection produced by a CRL with a perfect parabolic profile. The results clearly show that the CRL does not refract X-rays perfectly. In the case of a five-lens CRL (Fig. 4*b*) the error is minimized for the lens parameter R = 215 μm, which is larger than the design value R_t = 200 μm. The error also has a well defined profile reproducible independently of the diameter along which the error is computed, which suggests rotational symmetry.

The addition of another four lenses to the stack increases the refractive power of the CRL and reduces the value of R at which the error is minimized to 205 μm. The effective radius of curvature of the CRL is getting closer to the design value, albeit only for points which lie inside a circle of radius ∼200 μm. This might be explained by the theory developed by Pantell *et al.* (2001), which predicts that misalignment of unit lenses will be compensated as the number of lenses in the CRL increases. However, the outer part is still better approximated by a line with a slope corresponding to a CRL with R = 215 μm. As in the case of the five-lens CRL, the error has a profile that does not depend on the direction and coincides very well with the profile obtained from μCT imaging [dotted lines in Figs. 4(*b*) and 4(*c*)]. The observed $R > R_t$ is in good agreement with the results derived from CT examination, and confirms that an excessive amount of diamond was systematically removed by the laser at the peripheral part of unit lenses (Fig. 1).

The gradient vector field of refraction angles presented in Fig. 5(*a*) was used to retrieve the phase delays introduced by the CRL by solving the Dirichlet boundary problem (Gasilov

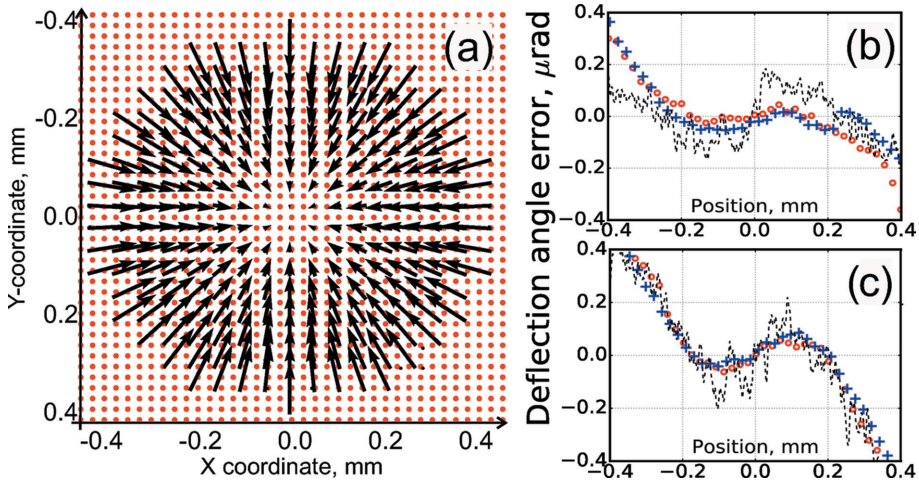

Figure 4
Deflection of X-rays by the CRL. 2D map of deflection angles in the exit plane of a nine-lens CRL (*a*); data for every second point is shown, the lengths of the vectors are proportional to the magnitude of the deflection. The deviation of the measured angles from ideal values produced by a CRL with a perfect parabolic profile is plotted for stacks of five (*b*) and nine lenses (*c*). Cross and circle markers show results along lines in the meridional and sagittal planes of the CRL. Errors for angles estimated from μCT are shown as dotted lines; the noisiness of these curves stems from the discretization of the CRL's projected thickness as discussed in §2.

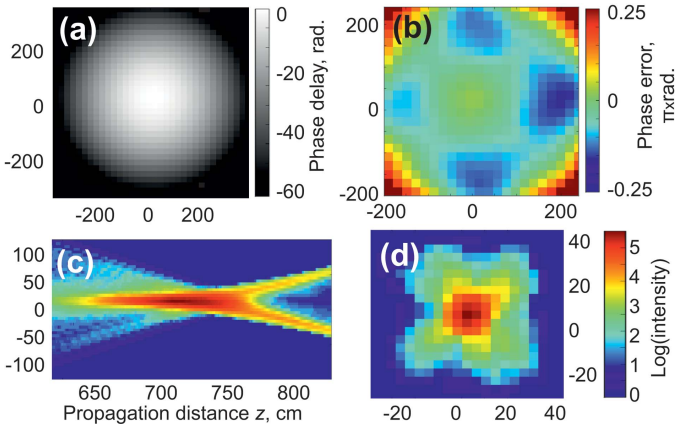

Figure 5
Reconstructed wavefront in the CRL exit plane (*a*); deviation of the wavefront from ideal parabolic profile (*b*). Propagation of the aberrated beam is simulated for 15 keV photon energy: section in the central vertical plane (*c*) and intensity of the beam computed in the plane z = 720 cm where the beam intensity reaches its maximum value (*d*). Unless specified, axes ticks indicate spatial coordinates in μm; panels (*c*) and (*d*) share a colorbar shown on their right.

et al., 2014). The results are shown Fig. 5(*a*). The phase difference $\Delta\phi(x, y)$ between the observed aberrated and the ideal parabolic wavefronts, with specific reference on the part of the CRL pupil where $|\Delta\phi| < \pi/4$, is reported in Fig. 5(*b*). At radial distances from the CRL optical axis lying in the range 100 μm $< r <$ 200 μm, the phase delay is somewhat smaller than expected from a perfect parabolic lens; it indicates that the projected thickness of diamond is increasing faster than necessary. At $r \simeq 200$ μm there is an inflection point and outside this circle $\Delta\phi(x, y)$ monotonically and rapidly increases in all radial directions; this signifies that an excessive amount of material is systematically removed at the periphery of unit lenses. The wavefront curvature is smaller than necessary, which will result in a shift of the focal spot (Wyant & Creath, 1992) from the expected position, similarly to the negative spherical aberration.

We also estimated the angular width of the focal spot produced by the CRL. As suggested in the *Introduction*, the optical properties of the examined CRL are evaluated for the 15 keV photon beam, which is close to the typical operation energy of a CRL. The measured phase delays are thus scaled inversely to the photon energy to set the boundary conditions for the simulation. It was assumed that the CRL is illuminated by a parallel incoherent X-ray beam. The CRL transmissivity was computed based on the NIST cross-section tables. Here we neglected the effects of scattering on sub-pixel size inhomogeneities to emphasize the influence of the wavefront aberrations on the CRL performance. The linear attenuation coefficient is then equal to $\mu = 2.82\ \mathrm{cm}^{-1}$, while $\delta = 3.38 \times 10^{-6}$. The propagation of the beam after the CRL is illustrated in Fig. 5(*c*). The beam intensity reaches its maximum value in the plane $z = 720 \pm 10$ cm, whereas the theoretical focal plane position for N plane-concave lenses is $z_t = R/N\delta = 680$ cm. The full width at half-maximum (FWHM) value of the beam intensity profile is minimized at ∼12 μm (Fig. 5*d*). Consequently, the angular dimensions of the focal spot, as it is seen from the lens, is ∼20 μm/7.2 m $\simeq$ 3 μrad. It is interesting to note that this spot encircles around 50% of the total intensity of the beam incident on the input aperture of the CRL.

5. Angular distribution of intensity in the beam transmitted through the CRL

In this section we analyze how the beam intensity in the lens exit plane is distributed at angles whose magnitudes are comparable with the angular width of the focal spot estimated in the previous section. We define, as a transmitted beam, the beam fraction propagating into a cone with opening angle equal to the analyzer crystal scanning range. Subsequently, we define here the transmission T_i as the ratio of the integrated intensities of the RC obtained with and without the lens. This parameter indicates how the beam intensity decreases due to the absorption, Compton scattering and elastic scattering to angles exceeding ±6 μrad. These lost photons either do not contribute to the focal spot at all or constitute a background halo around the focused beam. Fig. 6 compares T_i measured at 51 keV (solid line) against the transmission I/I_0 computed using the Beer–Lambert law and the tabulated cross sections of elementary interactions (dashed-dotted line). To estimate the latter, the diamond projected thickness is taken from the X-ray imaging experiment described in §2; the attenuation coefficient includes photo-absorption, Compton and coherent scattering terms as found in the NIST database. A difference between the two curves is expected if an appreciable amount of photons are lost due to small-angle scattering on micrometer-size fluctuations of the electron density. It can be seen that for one lens the relative difference is around 1%, which is comparable with the measurement error originating from the fluctuations of the X-ray beam intensity. In the case of nine lenses, the difference increases towards the peripheral part of the lens but does not exceed 2–3%. We can thus conclude that only a small fraction of the beam intensity is completely lost from the transmitted beam due to small-angle scattering at angles larger than the analyzed interval.

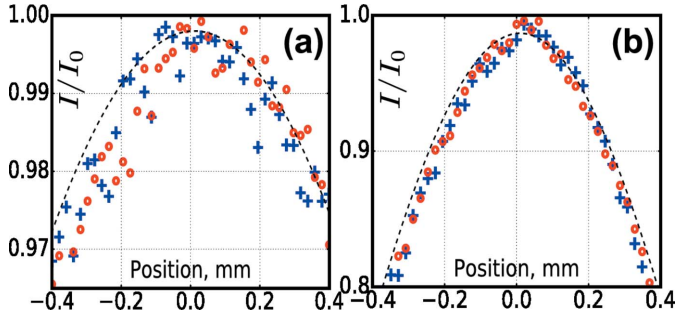

Figure 6
Measured lens transmission across the vertical and horizontal diameters of the CRL (cross and circle markers, respectively). The theoretical transmission calculated using the Beer–Lambert law is shown by dash-dotted lines. Panels (*a*) and (*b*) show the results for one lens and nine lenses, respectively.

We need to interpret now the rather complex profile of the intensity *versus* angle distribution, typical examples of which are reported in Figs. 2(*b*) and 2(*c*). First, the beam intensity is symmetrically dispersed at angles $\sim\pm1$ µrad around the transmitted beam, which can be detected as the broadening of the RC. This happens both when the transmitted beam is deflected (Fig. 2*c*) and when it does not change the propagation direction because it is located close to the CRL optical axis (Fig. 2*b*). Second, a significant fraction of the intensity beam transmitted through the peripheral part of the lens is smeared over the entire angular interval between the straight and the deflected beams. It is seen as a strong asymmetry in the RC tails (Fig. 2*c*). The latter effect can be explained considering that the beam loses a fraction of intensity upon propagation and refraction in each unit lens. In the general case, the angular distribution of scattered photons is symmetrical around the main beam (Beeman & Kaesberg, 1947). Photons lost in the first unit lens continue to propagate and interact with the rest of the lenses; however, their average propagation direction is biased towards the initial propagation direction. The same happens with photons lost in the second lens, but their angular distribution is less biased to the initial propagation direction than that of the first lost fraction, and so on. As a result of this process, cumulative angular distribution of the scattered photons is spread between the straight and the deflected beams. This effect is amplified as the number of lenses in the CRL increases. For instance, in the case of a five-lens stack, the $I_{\rm RC}$ distribution is only slightly skewed for points lying on a circle of radius $\sim$250 µm. However, in the case of a nine-lens stack, plenty of photons are found several half-widths away from the central maximum of the refracted beam. About 10–20% of the transmitted beam intensity is contained in the RC tail formed by the scattered photons. These photons are not completely extinct from the transmitted beam, but cannot contribute to the image formation either.

The symmetric component of RC broadening has a very weak dependence on the material thickness. Figs. 2(*b*) and 2(*c*) show that the FWHM of the curve measured at the lens center where the diamond thickness is $t < 0.3$ mm is similar to points at $r \simeq 260$ µm far from the center where $t \simeq 1.5$ mm. Since the number of intersected lens surfaces is the same for all points in the CRL pupil, we suggest that symmetric RC broadening stems from multiple refraction of X-rays. It can be viewed as the dispersion of the average propagation direction of the transmitted beam in each 20 µm × 20 µm wavefront sample due to the slight spatial variations of the incidence angle at different unit lenses. We quantified the associated increase of the transmitted beam angular width by measuring the increment of the RC variance. For a perfectly collimated beam the multiple refraction mechanism should give an intensity *versus* angle distribution of the form

$$I_{\rm RC}(\theta) = C\exp\left(-\theta^2/w^2\right), \qquad (1)$$

where w is proportional to the refractive index decrement multiplied by the square root of the number of interfaces traversed (Beeman & Kaesberg, 1947; Faris & Byer, 1988). Fig. 7 illustrates that the increment of the RC variance

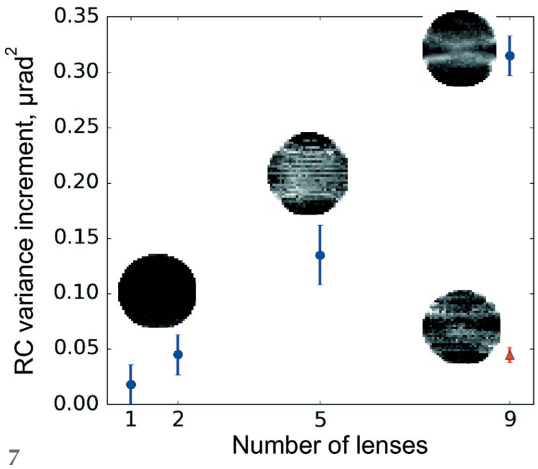

Figure 7
Increase of the RC fit variance *versus* number of lenses in the CRL. The insets show the two-dimensional distribution of broadening in a circle of radius 300 µm centered at the optical axis. The red triangle marker is the value measured at 90 keV. A suitable correction for systematic broadening that stems from averaging of deflection angles over the detector pixel dimensions is made (such broadening would be observed even in a perfect CRL).

increases linearly with the number of lenses. In addition, the ratio of variances measured at photon energies of 51 and 90 keV is $w_{51}^2/w_{90}^2 = 0.360/0.044 = 8.2$, indicating that w^2 scales almost as the fourth power of the photon energy, $(90/51)^4 = 9.6$. Deviation from the E^{-4} law may be explained by the increasing background of the scattered radiation, whose angular distribution width $w \simeq E^{-1}$ also shrinks at higher energies.

Because of the RC broadening, almost 20–25% of photons are spread at extremely small, but still significant, angles around the mean propagation direction of the transmitted beam. Correspondingly, the peak intensity of the transmitted beam decreases. Considering that w scales at least as E^{-1}, the angular spread of X-rays at each point in the CRL exit plane will increase by nearly 5 µrad at $E = 15$ keV with respect to the beam divergence at the CRL entrance plane. This fact alone must influence the spatial distribution of the intensity in the focal spot, even when surface errors and associated aberrations do not exist at scales exceeding the spatial resolution of the detector. To a good approximation the image of a point source would be simply blurred because of this ultra-small-angle broadening. The amount of blurring in spatial coordinates is proportional to the product of w and the propagation distance.

6. Discussion and summary

As mentioned in the *Introduction*, one of the primary applications of a single-crystal diamond CRL is focusing of intense X-ray beams. Considering that in many practical cases the spatial coherence of an X-ray beam illuminating a CRL is much smaller than the dimensions of the CRL entrance pupil, we examined the PSF of the studied CRL. The PSF is one of the main characteristics of any lens, which indicates the degree of blurring in the image of the point source. The narrower the

PSF, the larger the gain that can be achieved when CRLs are applied for focusing of undulator radiation. We estimated the PSF by applying the inverse Fourier transform to the auto-correlation of the generalized pupil function $P = T\exp(i\phi)$, where $T = \sqrt{T_i}$ is the amplitude transmission and φ is the wavefront aberration (Goodman, 2005). It is assumed that a circular aperture of radius 300 µm blocks the peripheral part of the CRL pupil in all PSF calculations. Fig. 8(*a*) presents PSF_{gen} of the examined nine-lens stack estimated for E = 15 keV by taking into account the wavefront aberrations measured in §4 and neglecting the ultra-small-angle scattering effects discussed in §5. The horizontal one-dimensional profile of the resulting PSF_{gen} is shown in Fig. 8(*b*) by the solid blue line. The full width of the PSF_{gen} central peak is nearly twice as large as the width of the PSF estimated solely from the CRL transmission (dashed red line).

Detected angular broadening in the transmitted beam should also blur the focal spot and reduce the gain. Results indicate that the divergence of a 15 keV pencil-like beam after its propagation through the CRL will be increased by at least 5 µrad. Upon propagation to the CRL focal plane $z \simeq 7$ m, the intensity of such a pencil-like beam will be spread over a spot of diameter $b \simeq 40$ µm. The image of a point source will be blurred by the same amount. In general, the width of the PSF will be increased proportional to the measured broadening of the RC profiles and the focal length. One way to take into account additional blurring induced by ultra-small-angle scattering is to convolve the PSF with the Gaussian-shaped curve, whose FWHM is equal to b. The resulting estimate for PSF_{usaxs} is shown in Fig. 8(*c*) by a dotted line. Observed ultra-small-angle scattering can reduce the gain by a factor of three to four compared with the value estimated from the CRL transmission only. It is worth noting that, while the large-scale surface errors can be eliminated by improving the precision of the micromachining process, the observed redistribution of the intensity in a very narrow cone around the forward direction will still limit the quality of the CRL. The latter effect is related to the microstructure of the diamond surface after interaction with ultra-fast laser pulses. The residual roughness could not be decreased by a simple polishing or chemical treatment.

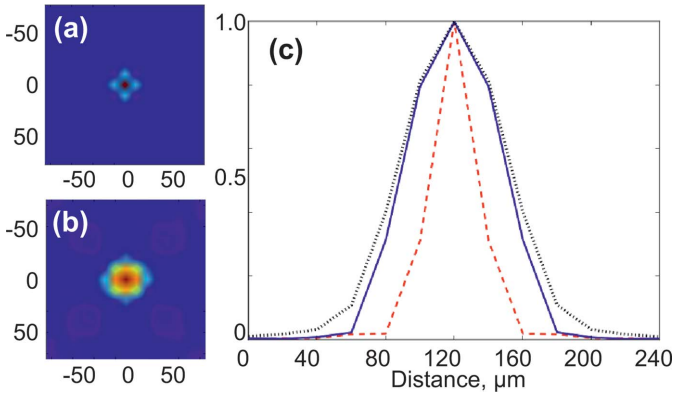

Figure 8
The point spread function (PSF) of the single-crystal diamond CRL calculated for 15 keV photon energy based on: the CRL transmission only [panel (*a*) and dashed line in (*c*)] and the generalized pupil function [panel (*b*) and solid blue line in (*c*)]. Lines in panel (*c*) show one-dimensional profiles of the PSF across the horizontal line intersecting the PSF maximum. The dotted line shows the estimation of the PSF after having taken into account the ultra-small angular broadening of the beam. Axes ticks at the edges of panels (*a*) and (*b*) specify the spatial coordinates in µm.

In conclusion, we have measured angular distributions of intensity in an X-ray beam transmitted through a single-crystal diamond CRL as a function of spatial coordinates in the CRL exit plane. The experiment was performed by means of a double-crystal setup. This technique allows measurement of strong wavefront curvatures in X-ray beams with spatial resolution of 10–20 µm. At 51 keV the setup of the ESRF ID17 beamline can measure X-ray angular deflections up to ±30 µrad, which is equivalent to ±300 µrad for a metrology setup operating at 15 keV. That might be useful if a direct characterization of the refractive properties of a CRL composed of many tens of unit lenses is in question. Also, despite the angular range of measurements being confined to a very narrow forward cone, the method yields important information about the influence of scattering on the CRL properties. We believe that the described approach can be fruitfully applied to the characterization of compound refractive lenses and, possibly, other X-ray optical elements.

Acknowledgements

We would like to acknowledge the ESRF for provision of beam time through proposals MD912 and IH1227. Thanks are due to T. Farago for his help with wave-optics simulations of the beam propagation.

References

Antipov, S., Baryshev, S. V., Butler, J. E., Antipova, O., Liu, Z. & Stoupin, S. (2016). *J. Synchrotron Rad.* **23**, 163–168.
Beeman, W. W. & Kaesberg, P. (1947). *Phys. Rev.* **72**, 512.
Faris, G. W. & Byer, R. L. (1988). *Appl. Opt.* **27**, 5202–5212.
Gasilov, S., Mittone, A., Brun, E., Bravin, A., Grandl, S., Mirone, A. & Coan, P. (2014). *Opt. Express*, **22**, 5216–5227.
Goodman, J. W. (2005). *Introduction to Fourier Optics*, 3d ed., §6.4.1. Englewood: Roberts.
Koch, F. J., Detlefs, C., Schröter, T. J., Kunka, D., Last, A. & Mohr, J. (2016). *Opt. Express*, **24**, 9168–9177.
Kolodziej, T., Vodnala, P., Terentyev, S., Blank, V. & Shvyd'ko, Y. (2016). *J. Appl. Cryst.* **49**, 1240–1244.
Lengeler, B., Tümmler, J., Snigirev, A., Snigireva, I. & Raven, C. (1998). *J. Appl. Phys.* **84**, 5855–5861.
Nardroff, R. von (1926). *Phys. Rev.* **28**, 240–246.
Pantell, R. H., Feinstein, J., Beguiristain, H. R., Piestrup, M. A., Gary, C. K. & Cremer, J. T. (2001). *Rev. Sci. Instrum.* **72**, 48–52.
Parratt, L. G., Porteus, J. O., Schnopper, H. W. & Watanabe, T. (1959). *Rev. Sci. Instrum.* **30**, 344–347.
Piestrup, M. A., Cremer, J. T., Beguiristain, H. R., Gary, C. K. & Pantell, R. H. (2000). *Rev. Sci. Instrum.* **71**, 4375–4379.
Rutishauser, S., Zanette, I., Weitkamp, T., Donath, T. & David, C. (2011). *Appl. Phys. Lett.* **99**, 221104.
Seiboth, F., Kahnt, M., Scholz, M., Seyrich, M., Wittwer, F., Garrevoet, J., Falkenberg, G., Schropp, A. & Schroer, C. G. (2016). *Proc. SPIE*, **9963**, 99630P.
Seiboth, F., Schropp, A., Scholz, M., Wittwer, F., Rödel, C., Wünsche, M., Ullsperger, T., Nolte, S., Rahomäki, J., Parfeniukas, K., Giakoumidis, S., Vogt, U., Wagner, U., Rau, C., Boesenberg, U.,

Garrevoet, J., Falkenberg, G., Galtier, E. C., Ja Lee, H., Nagler, B. & Schroer, C. G. (2017). *Nat. Commun.* **8**, 14623–14628.
Semenov, A. A., Zabrodin, A. V., Gorlevskiy, V. V., Sheverdyaev, M. S., Lizunov, A. V., Brylev, D. A., Anikin, A. S., Klykov, S. S., Kozlova, E. V., Lesina, I. G., Nebera, A. L., Morozov, I. A., Demin, A. V., Buzmakov, A. V., Dymshicz, Y. M., Volkov, V. V., Zhigalina, O. M., Konarev, P. V., Khmelenin, D. N., Seregin, A. V., Senin, R. A., Roshchin, B. S. & Asadchikov, V. E. (2017). *Crystallogr. Rep.* **62**, 25–30.
Slack, C. M. (1926). *Phys. Rev.* **27**, 691–695.
Snigirev, A., Kohn, V., Snigireva, I., Souvorov, A. & Lengeler, B. (1998). *Appl. Opt.* **37**, 653–662.
Snigirev, A., Yunkin, V., Snigireva, I., Di Michiel, M., Drakopoulos, M., Kouznetsov, S., Shabel'nikov, L., Grigoriev, M., Ralchenko, V., Sychov, I., Hoffmann, M. & Voges, E. I. (2002). *Proc. SPIE*, **4783**, 1–9.
Stepanov, S. A. (2004). *Proc. SPIE*, **5536**, 16–26.
Stöhr, F., Simons, H., Jakobsen, A. C., Nielsen, C. H., Michael-Lindhard, J., Jensen, F., Poulsen, H. F., Hansen, O. & Hübner, J. (2015). *Opt. Mater. Expr.* **5**, 2804–2811.
Terentyev, S., Blank, V., Polyakov, S., Zholudev, S., Snigirev, A., Polikarpov, M., Kolodziej, T., Qian, J., Zhou, H. & Shvyd'ko, Y. (2015). *Appl. Phys. Lett.* **107**, 111108.
Terentyev, S., Polikarpov, M., Snigireva, I., Di Michiel, M., Zholudev, S., Yunkin, V., Kuznetsov, S., Blank, V. & Snigirev, A. (2017). *J. Synchrotron Rad.* **24**, 103–109.
Weitkamp, T., Nöhammer, B., Diaz, A., David, C. & Ziegler, E. (2005). *Appl. Phys. Lett.* **86**, 054101.
Wernick, M. N., Wirjadi, O., Chapman, D., Zhong, Z., Galatsanos, N. P., Yang, Y., Brankov, J. G., Oltulu, O., Anastasio, M. A. & Muehleman, C. (2003). *Phys. Med. Biol.* **48**, 3875–3895.
Wyant, J. C. & Creath, K. (1992). *Appl. Opt. Opt. Eng.* **11**, 2–53.